Optical near-field Raman imaging with subdiffraction resolution

Pietro G. Gucciardi, Sebastiano Trusso, Cirino Vasi, Salvatore Patanè, and Maria Allegrini

We report optical near-field Raman imaging with subdiffraction resolution (~120 nm) without field enhancement effects. Chemical discrimination on tetracyanoquinodimethane organic thin films showing localized salt complexes is accomplished by detailed Raman maps. Acquisition times that are much shorter than previously reported are due to the high Raman efficiency of the materials and to a careful collection and detection of the optical signals in our near-field Raman spectrometer.

OCIS codes: 180.0180, 180.5810, 300.0300, 300.6450.

1. Introduction

The combination of near-field scanning optical microscopy (NSOM)[1,2] techniques with Raman spectroscopy represents a step forward into materials phase analysis, chemical recognition, and local stress measurements at the nanometer scale. NSOM-Raman (nano-Raman) spectroscopy with use of optical fibers as probes[3] is, however, challenging because the Raman scattering is an extremely inefficient process, and the amount of light available for sample excitation is limited. The throughput of metallized NSOM probes is, in fact, very low ($\sim 10^{-5}$ for 50-nm apertures), and thermal burning of the metal coating occurs for input laser powers larger than ~10 mW. Efforts to achieve nano-Raman imaging are thus justified if an advantage in terms of lateral resolution can be demonstrated with respect to standard confocal micro-Raman investigations. The limit to be overcome is established by the Abbe criterion[4]: $0.61\ \lambda/\mathrm{NA}$. For light at $\lambda = 514.5$ nm, it roughly varies from 300 nm with dry microscope objectives (NA = 0.95), to 240 nm for samples allowing the use of immersion oil objectives (NA = 1.3).

The first Nano-Raman spectra were carried out by Tsai *et al.*[5] on diamond particles. Nano-Raman maps of rubidium-doped $KTiOPO_4$ crystals were reported,[6,7] and subsequently different selection rules holding in far- and near-field Raman spectroscopy were pointed out.[8] Nano-Raman imaging was also demonstrated on silicon samples to map the stress distribution[9,10] occurring in proximity of a surface defect. In those experiments, pulled metal-coated NSOM fiber probes were used to locally excite the sample, collecting the backscattered light through long working distance objectives. Spectral resolution better than 10 cm^{-1} was reported, with acquisition times of ~10 h to carry out maps of a few tens of points per line. Because of the poor signal-to-noise (S/N) ratio, resolution assessments were based on estimates of the probe aperture and not on quantitative evaluations (e.g., line profiles) of the Raman images. To increase the S/N ratio and to reduce the integration time to reasonable values, resonant Raman enhancement[11,12] and surface-enhanced Raman scattering (SERS) were proposed. Spectra of Rhodamine molecules adsorbed on silver nanoparticles substrates demonstrated[13–15] enhancement factors of $\sim 10^{13}$, and the combination of SERS with high-throughput fiber probes[16,17] provided the first proof of subdiffraction resolution Nano-Raman imaging (100 nm) of dye-labeled DNA molecules.[18] Nevertheless, long integration times (~6 h) were necessary for the acquisition of 20×20 points maps. More recently, apertureless-NSOM configurations, providing tip-induced local field enhancement, have been adopted,[19] in combination with SERS[20,21] or in photon-

P. G. Gucciardi, S. Trusso, and C. Vasi are with the Consiglio Nazionale delle Richerche, Istituto per i Processi Chimico-Fisici, sez. Messina, Via La Farina 237, I-98123, Messina, Italy. S. Patanè is with the Istituto Nazionale per la Fisica della Materia, Dipartimento di Fisica della Materia e Tecnologie Fisiche Avanzate, Università di Messina, Salita Sperone 31, I-98166 Messina, Italy. M. Allegrini is with the Istituto Nazionale per la Fisica della Materia, Dipartimento di Fisica, Università di Pisa, Via F. Buonarroti 2, I-56127, Pisa, Italy.

Received 17 September 2002; revised manuscript received 20 January 2003.

0003-6935/03/152724-06$15.00/0

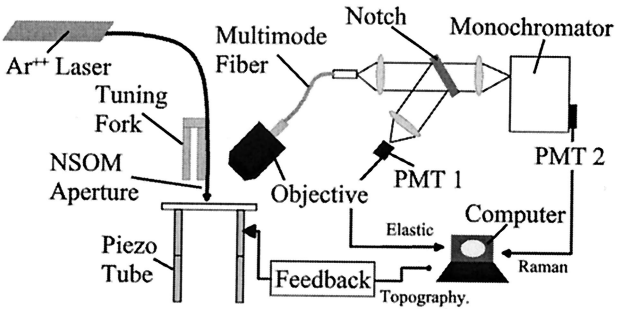

Fig. 1. Schematic of the nano-Raman setup.

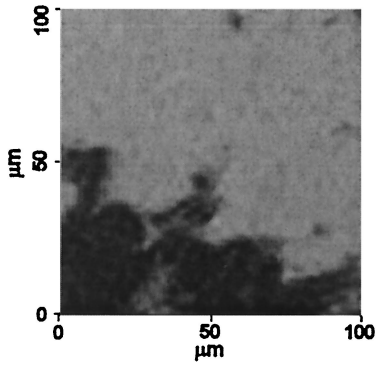

Fig. 2. Microphoto of the tetracyanoquinodimethane (TCNQ) thin film. The dark areas are due to the strong absorption of the coppersalt (CuTCNQ) complexes.

scanning tunneling configurations.[22] Spectral inhomogeneities have been observed on lateral scales of a few tens of nanometers on samples consisting of thin molecular layers.

In this paper we show for the first time that, within a class of high Raman efficiency organic materials, it is possible to achieve subdiffraction resolution nano-Raman imaging, without the need of field enhancement effects. Our setup exploits commercially available fiber probes. On the basis of the reflection mode configuration, it overcomes the need of transparent samples.

2. Experimental Setup

Figure 1 shows the setup based on our previous NSOM design[23] and implemented for Raman spectroscopy.[24] The compact design plus an efficient vibration isolation system makes the instrument very stable, with drifts smaller than 50 nm/h. The 514.5-nm line of an Ar^+ laser is coupled to a NSOM probe (Nanonics Ltd., nominal aperture $a \sim 100$ nm) to illuminate the sample. Nonoptical shear force[25,26] detection is accomplished by means of a quartz tuning fork[27] externally dithered by a piezo slab. The scattered light is collected through a high-numerical-aperture, long working distance objective (NA = 0.5, WD = 10.6 mm) resting at 45° with respect to the probe axis and coupled to a multimode fiber (core diameter, 200 μm) by means of a connectorized lens package. The light is thus collimated and focused onto the slits of a monochromator. A notch filter (rejection ratio $> 10^6$) reflects back the elastically scattered light, which is subsequently detected by a photomultiplier (PMT 1), providing the elastic scattering signal. We use a single grating monochromator (190-mm focal length, 1200 lines/mm, blazed at 500 nm) which provides high luminosity, despite a poor spectral resolution (0.3 nm). A further photomultiplier (PMT 2), operating in photon counting mode, has been preferred because of its high sensitivity at low-light levels. The Raman signal is thus acquired simultaneously to the topography and the elastic scattering.

3. Results and Discussion

As a test sample we have chosen 7,7′,8,8′-tetracyanoquinodimethane (TCNQ), which is a very efficient Raman scatterer. TCNQ is a strong electron acceptor and forms a variety of charge-transfer (CT) complexes with inorganic and organic donors. These compounds have recently attracted the attention of both physicists and chemists as dopant materials in organic optoelectronic devices.[28,29] Our sample is a TCNQ thin film (thickness ~1 μm) grown by ultra-high-vacuum thermal deposition on a KBr substrate. After deposition, the sample was covered with a fine copper powder and stored at 40 °C for about one month. The yellow surface was thus populated by a number of blue spots indicating the presence of localized CT copper-salt (CuTCNQ) aggregates. The CT transition yields a strong absorption band in the visible spectrum and causes frequency perturbations in the optical vibration spectra.

The strong absorption of the CuTCNQ is responsible for the dark areas visible in Fig. 2, displaying a microphotograph of the sample surface (100×100 μm^2). We observe that the sample is microstructured with spots of some tens of micrometers and a few smaller areas only a few micrometers wide. A more detailed elastic scattering image [Fig. 3(a), 10×10 μm^2] has been carried out by NSOM means on a border area in order to image both chemical compounds. In the darker area (indicated with the letter B) the signal is attenuated by approximately 1 order of magnitude with respect to that measured at positions A and C, indicating the presence of a strongly absorbing material such as could be the CuTCNQ. No clear correlations with the topography map[24] have been observed down to the submicron scale, assessing the genuine nature of the elastic scattering signal. To support the conclusion about the chemical nature of the materials, nano-Raman spectra have been acquired on the sites A and B. The site A spectrum [Fig. 3(c), top plot, gray line] displays the chemical fingerprint of the neutral TCNQ[30] with the most intense peaks at 1453 cm^{-1} (C = C wing stretching), 1196 cm^{-1} (C = C–H bending), 1600 cm^{-1} (C = C ring stretching), and 2221 cm^{-1} (C ≡ N stretching) superimposed to a elastic stray light background (TCNQ does not show fluorescence in this spectral region[30]). A clear shift of the 1453-cm^{-1} peak towards 1381 cm^{-1} appears in the site B spectrum [Fig. 3(c), bottom plot], proving the salt occur-

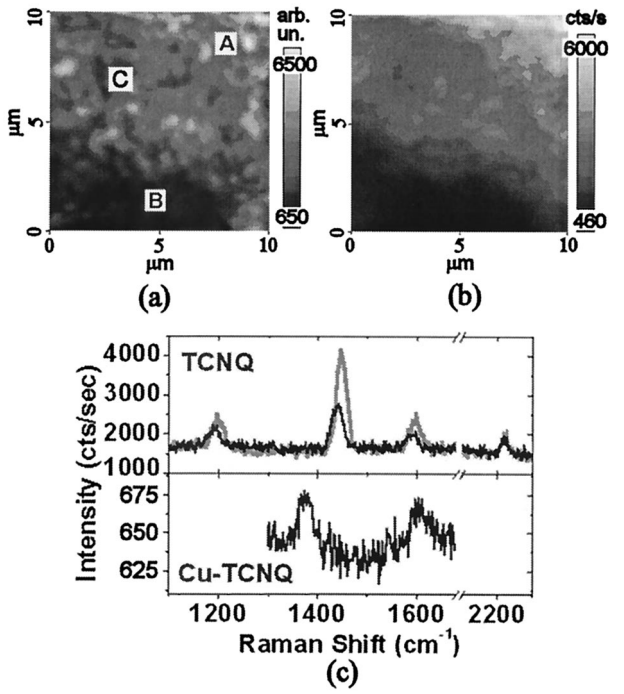

Fig. 3. (a) Elastic and (b) Raman scattering map at 1453 cm^{-1} acquired on a border between a TCNQ-rich area (indicated with the letters A and C) and a CuTCNQ cluster (letter B). The Raman spectra, shown in the top plot of (c), were acquired respectively at positions A (light gray curve) and C (black curve) within the TCNQ-rich area. They display the typical TCNQ peaks with different intensities superimposed to a constant background. In the spectrum acquired at position B [bottom plot of (c)] we see the shift of the 1453-cm^{-1} peak toward 1381 cm^{-1}, representing the chemical fingerprint of the CuTCNQ compound.

rence[30] in this area. The overall strong attenuation of the Raman signal observed therein, in addition to the reduction of the intensity ratio between the two peaks at 1453 and 1600 cm^{-1} are in agreement with independent micro-Raman investigations.[24,30] The TCNQ Raman spectrum was obtained with ~100-nW excitation power and an integration time $\tau = 300$ ms per point, assessing the possibility to perform nano-Raman imaging in reasonable times. Differently, the CuTCNQ spectrum required an integration of 5 s per point to evidence the frequency shift with an appreciable S/N ratio. Spectra carried out in this zone with shorter integration times (~100 ms) only yielded a noisy background of ~500 counts/second (cts/sec) with no spectral features, while the peaks were well visible when moving back into the TCNQ zone.[24] A spectral resolution of 28 cm^{-1} comes out from the FWHM of the peaks. Pure chemical discrimination of the two materials can thus be accomplished by mapping the intensity pattern of the C = C wing-stretching mode of the TCNQ (1453 cm^{-1}). This is true since (1) the corresponding vibrational mode of the CuTCNQ is shifted ($\Delta E = 72$ cm^{-1}) beyond the acquisition spectral window, determined by the monochromator resolution; and (2) differently from the TCNQ, the Raman activity of the CuTCNQ falls below the noise threshold when setting subsecond integration times. In Fig. 3(b) we display the nano-Raman map at 1453 cm^{-1} (128 × 128 points) carried out simultaneously to the elastic scattering image of Fig. 3(a), setting $\tau = 100$ ms per point. The map was thus obtained in less than 1 h (we acquired the signals during both the scan directions). The vanishing of the Raman activity in the site B supports the conclusions drawn before about the occurrence of a large CuTCNQ aggregate. Spatial modulations of the Raman activity can be observed within the TCNQ rich zone (sites A and C) on subwavelength scales. The pure chemical nature of the contrast observed therein is confirmed by comparing the Raman spectra [Fig. 3(c), top plot] acquired at positions A (gray line) and C (black line) showing that only the peak's intensity does change, without any appreciable variation of the background baseline. On the other hand, in the transition from regions A and C to region B we see a reduction of the background of ~850 cts/s (from 1500 to 650 cts/s) but the overall signal is indeed dominated by the Raman contribution, which drops by more than 1 order of magnitude, passing from a maximum value of ~6000 cts/s to the noise level (~450 cts/s).

To provide evidence of subdiffraction resolution, we have moved to a different zone showing fluctuations of the Raman activity on smaller-length scales. Most of the same experimental conditions were maintained in this measurement ($\tau = 100$ ms, smaller excitation power). In Fig. 4 we show a three-dimensional rendering of (a) the topography, (b) the elastic scattering image, and (c) the Raman map at 1453 cm^{-1}, all simultaneously acquired (2.4 × 2.0 μm^2, 123 × 102 points). On the upper left-hand corner we can see part of a bumplike structure having dimensions in the micrometer scale and ~400 nm height. This structure is characterized by a high elastic [Fig. 4(b)] and Raman scattering [Fig. 4(c)], suggesting the occurrence of a TCNQ-rich aggregate, which did not react with the copper. The central part of the Raman map instead displays the formation of round-shaped CuTCNQ complexes [appearing in Fig. 4(c) as elongated structures because of perspective reasons] whose dimensions (FWHM of 235, 158, and 146 nm) can be determined from the line profile shown in Fig. 4(f) (top plot). With the help of the shaded boxes (a guide to the eye used to reproduce the dimensions and location of salt complexes) we can see that the corresponding line profile carried out on the elastic scattering map [Fig. 4(e), top plot] shows broader features, slightly shifted (~100 nm) with respect to those observed in the Raman profile. A completely different pattern can be seen in the topography profile [Fig. 4(d), top plot]. On the right-hand side of the Raman map is a smaller high-intensity spot (circled), having lateral dimensions of ~700 nm, indicating the occurrence of a TCNQ-rich area. Contrary to the previous structure, this one does not have a counterpart either in the topography or in the elastic scattering map, showing a different spatial modulation [as indicated by the white arrows in Figs. 4(a), 4(b)]. The decrease of the Raman scat-

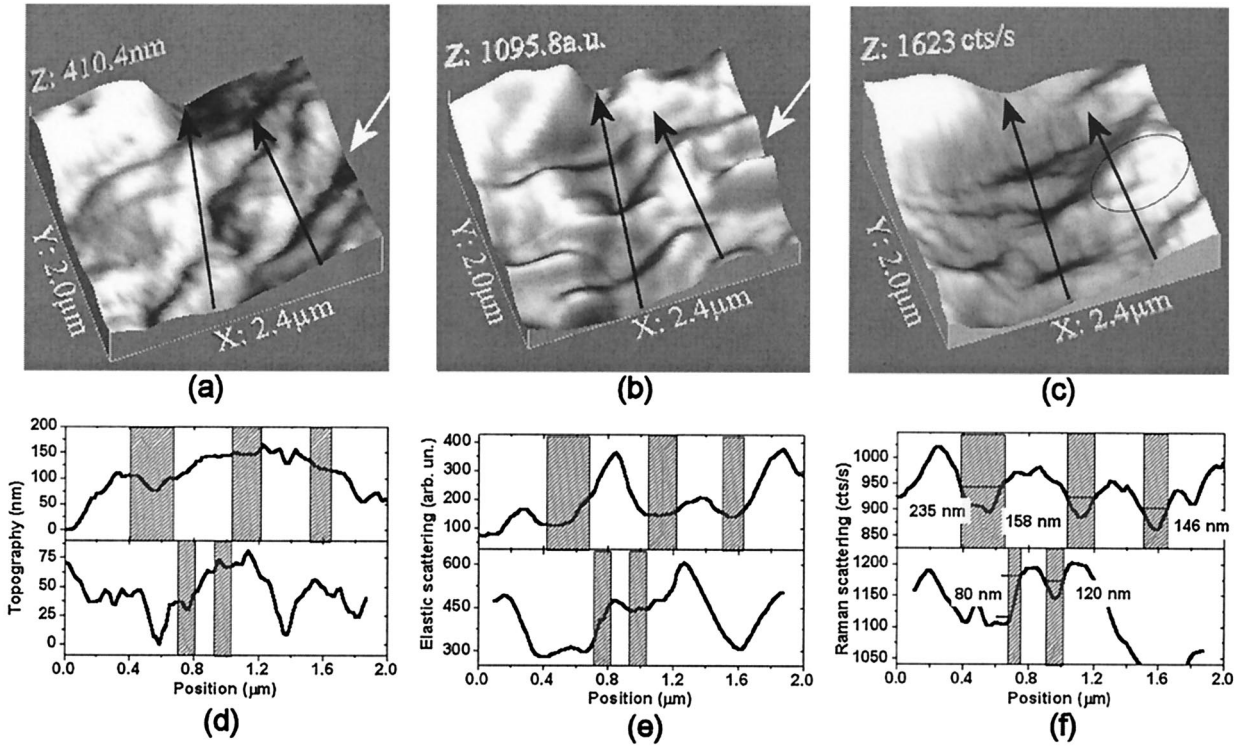

Fig. 4. (a) Topography, (b) elastic scattering, and (c) Raman map at 1453 cm^{-1}. The arrows indicate from where the line profiles reported in (d), (e), and (f) have been extracted (the top plots refer to the left-hand side arrow, the bottom plots to the right hand side one). The patterned boxes are a guide to the eye to point out that no correlation exists between the three signals in those sites used to assess the nano-Raman spatial resolution.

tering, visible inside this spot, is due to the local presence of CuTCNQ; the Raman line profile [related to the right-hand arrow of Fig. 4(c)] reported in Fig. 4(f) (bottom plot) allows us to assess a lateral dimension of 120 nm for the salt cluster as well as to observe a transition between two sites with different copper contamination (signal variation ~8%), occurring within 80 nm (10–90% criterion).

A different chemical morphology has been observed on a further zone, showing a bump-like structure. In Fig. 5 we report the topography (top), the Raman at 1453 cm^{-1} (center), and the elastic scattering (bottom) line profiles extracted from a line scan map (10-μm length, 128 points), carried out by changing the detection energy while scanning the same line. Contrary to what is reported in Fig. 4, we can observe the reduction of the Raman intensity on top of the bump (~3000 cts/s), with respect to the surroundings (>5000 cts/s). This behavior proves the presence of a layer of CuTCNQ on top of this structure. We can note that the Raman profile does not show the strong modulations visible in the elastic scattering, and furthermore we observe that the two high intensity peaklike structures are shifted by ~500 nm with respect to each other. The latter effect is real and not due to drifts, accounted for by comparing the respective topography profiles.

We can extract valuable information about the local depth of copper contamination by a careful analysis of the different behavior of the Raman contrast observed in Figs. 3 and 4. The vanishing of the Raman signal observed in the site B of Fig. 3, in addition to the shift of the spectral emission and the intense

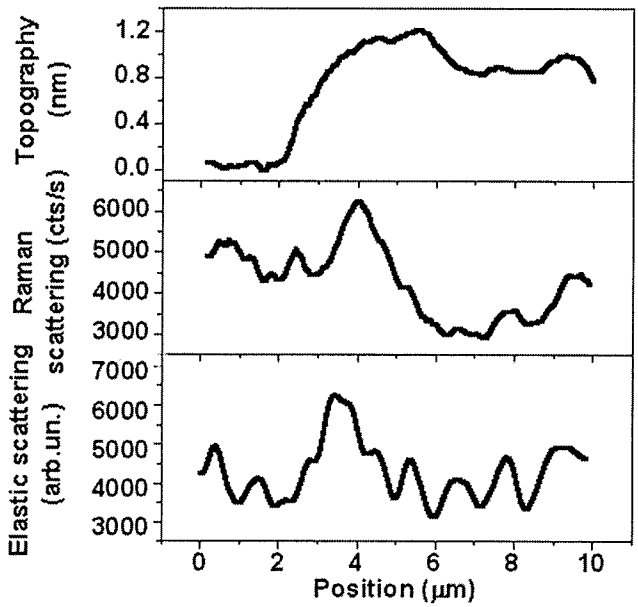

Fig. 5. Topography (top), Raman scattering at 1453 cm^{-1} (center), and elastic scattering (bottom) line profiles carried out on another bumplike structure showing a different chemical morphology with respect to that reported in Fig. 4.

absorption displayed by the elastic scattering map, provide clear evidence of a deep copper contamination. Quantitatively this means that, if we assume a sample thickness probed by the NSOM tip to be of the order of the near-field penetration depth ($\sim a \cong 100$ nm), the CuTCNQ spot thickness within site B will result to be $\gg$100 nm. On the other hand, the intensity modulations of the TCNQ Raman lines observed within sites A and C of Fig. 3(b), as well as in Fig. 4(c), and on top of the bump of Fig. 5 can be explained assuming the occurrence of thinner CuTCNQ layers, characterized by a thickness smaller than the near-field penetration depth. In this case, in fact, the probed volume will contain a residual layer of TCNQ, whose Raman emission, however, will be weakened by the occurrence of the surface CuTCNQ layer.

A further effect of the small absorption taking place in correspondence of thin CuTCNQ layers can explain the loss of correlation between the Raman and elastic scattering maps. The elastic scattering signal, in fact, carries information about the refractive index and the absorption coefficient but also contains contributions related to the surface morphology and topography artifacts.[31,32] Thus, as far as the absorption gives the main contribution to the optical signal, we expect a strong correlation between the elastic scattering and the Raman maps, as observed in Fig. 3 at the micrometer scale (sites A and B). Conversely, where different contributions prevail over the absorption to generate the total elastic scattering signal, we can expect a different spatial pattern with respect to the Raman one. This phenomenon is visible both in Fig. 3 (submicrometer features inside site A) and in Fig. 4 and is highlighted in more detail by the line profiles [Figs. 4(e), 4(f), and 5].

Artifacts are an important issue to take into account when discussing NSOM images. With this term we usually identify unwanted cross talks taking place among the different acquired signals, making their interpretation very difficult. An example is given by the so-called topography (or z-motion) artifacts[31,32] yielding optical maps very similar to their topographic counterpart. Geometric shadowing[33] represents a different kind of artifact that correlates the topography with the optical signals in a nontrivial way. Recently this issue has been discussed in detail in the papers by Stöckle *et al.*[15] and Deckert *et al.*,[18] who normalized the Raman signal to the reflectivity (elastic scattering) one, in order to get rid of geometry influences. This procedure is based on the observation that shadowing, as a geometric effect, affects both signals in a similar fashion. The normalization, however, is appropriate only if the sample is homogenous and shows fluctuations neither of the refractive index nor of the absorption coefficient; in this case, in fact, the reflectivity modulations can be attributed to pure geometric factors, which can thus be retrieved and used to correct the Raman signal. Conversely, the use of such normalization is not fully justified if relevant variations of the optical parameters take place, or if z-motion artifacts cannot be neglected, causing the reflectivity signal to vary independently from local geometry. z-motion artifacts, for example, are a coherent effect (interference) affecting the elastic scattering images that does not have a straightforward counterpart in the inelastic scattering image (photoluminescence or Raman). A normalization of the Raman signal, in this specific case, would be unphysical.

In our case the optical constants of the two materials are strongly different. We thus prefer to afford this issue starting from the more general principles that, whatever their origin, artifacts produce fictitious patterns exactly correlated in space (no shifts) and with the same spatial resolution.[31] While the occurrence of classical z-motion artifacts on the optical signals can be excluded (since the spatial patterns are completely different), two causes still could produce fictitious effects in our Raman maps: geometrical shadowing effects and the presence of the stray light background visible in the Raman spectra. In both cases, however, the elastic scattering and the Raman maps should be strongly correlated both at the micrometer and at the subdiffraction-length scales. The quantitative analysis of the profiles, conversely, shows lateral shifts and different dimensions of the structures at the subwavelength scale, proving the genuine nature of the Raman signal. On larger scales, the spectral analysis supports the conclusions based on the Raman images. In particular, the different spectral fingerprints observed in Fig. 3(c) between sites A and C prove the occurrence of different chemical species; moreover, the constant background level [Fig. 3(c), top plot] observed when moving from point A to point C, characterized instead by a different Raman activity, proves the absence of cross talks between the two maps. Finally the different behavior of the Raman signal observed in correspondence of the two bumplike structures (Figs. 4 and 5), prove the absolute independence between the topography and the Raman signal.

4. Conclusions

In summary, we have demonstrated chemical discrimination of different organic species on subdiffraction-length scales by using aperture-NSOM Raman techniques without taking advantage of field enhancement. A good S/N ratio has been achieved with unprecedented short integration times, owing to the high efficiency of the materials.

Support by Ministero dell'Università e della Ricerca Scientifica e Tecnologica within the Cluster C26, project no. 7 is greatly acknowledged.

References

1. D. W. Pohl, W. Denk, and M. Lanz, "Optical stethoscopy: image recording with resolution $\lambda/20$," Appl. Phys. Lett. **44,** 651–653 (1984).
2. A. Lewis, M. Isaacson, A. Harootunian, and A. Muray, "Development of a 500-Å spatial resolution light microscope," Ultramicroscopy **13,** 227–232 (1984).
3. E. Betzig, J. K. Trautman, T. D. Harris, J. S. Weiner, and R. L.

Kostelak, "Breaking the diffraction barrier: optical microscopy on a nanometric scale," Science **251,** 1468–1471 (1991).
4. E. Abbe, "Beiträge zur Theorie des Mikroskops und der Mikroskop ischen Wahrnehmung," Arch. Mikrosk. Anat. **9,** 413–418 (1873).
5. D. P. Tsai, A. Othonos, M. Moskovits, and D. Uttamchandani, "Raman spectroscopy using a fiber optic probe with subwavelength aperture," Appl. Phys. Lett. **64,** 1768–1770 (1994).
6. C. L. Jahncke, M. A. Paesler, and H. D. Hallen, "Raman imaging with near-field scanning optical microscopy," Appl. Phys. Lett. **67,** 2483–2485 (1995).
7. C. L. Jahncke, H. D. Hallen, and M. A. Paesler, "Nano-Raman spectroscopy and imaging with near-field scanning optical microscope," J. Raman Spectrosc. **27,** 579–586 (1996).
8. E. J. Ayars, H. D. Hallen, and M. A. Paesler, "Electric field gradient effects in Raman spectroscopy," Phys. Rev. Lett. **85,** 4180–4183 (2000).
9. S. Webster, D. N. Batchelder, and D. A. Smith, "Submicron resolution measurement of stress in silicon by near-field Raman spectroscopy," Appl. Phys. Lett. **72,** 1478–1480 (1998).
10. S. Webster, D. A. Smith, and D. N. Batchelder, "Raman microscopy using a scanning near-field optical probe," Vib. Spectrosc. **18,** 51–59 (1998).
11. A. C. Ferrari and J. Robertson, "Resonant Raman spectroscopy of disordered, amorphous, and diamond-like carbon," Phys. Rev. B **64,** 075414–075426 (2001).
12. D. A. Smith, S. Webster, M. Ayad, S. D. Evans, and D. N. Batchelder, "Development of a scanning near-field optical probe for localized Raman spectroscopy," Ultramicroscopy **61,** 247–252 (1995).
13. S. R. Emory and S. Nie, "Near-field surface-enhanced Raman spectroscopy on single silver nanoparticles," Anal. Chem. **69,** 2631–2635 (1997).
14. D. Ziesel, V. Deckert, R. Zenobi, and T. Vo-Dinh, "Near-field surface-enhanced Raman spectroscopy of dye molecules adsorbed on silver island films," Chem. Phys. Lett. **283,** 381–385 (1998).
15. R. M. Stöckle, V. Deckert, C. Fokas, D. Ziesel, and R. Zenobi, "Sub-wavelength Raman spectroscopy on isolated silver islands," Vib. Spectrosc. **22,** 39–48 (2000).
16. P. Lambelet, A. Sayah, M. Pfeffer, C. Philipona, and F. Marquis-Weible, "Chemically etched fiber tips for near-field optical microscopy: a process for smoother tips," Appl. Opt. **37,** 7289–7292 (1998).
17. R. M. Stöckle, C. Fokas, V. Deckert, R. Zenobi, B. Sick, B. Hecht, and U. P. Wild, "High-quality near-field optical probes by tube etching," Appl. Phys. Lett. **75,** 160–162 (1999).
18. V. Deckert, D. Ziesel, R. Zenobi, and T. Vo-Dinh, "Near-field surface-enhanced Raman imaging of dye-labeled DNA with 100-nm resolution," Anal. Chem. **70,** 2646–2650 (1998).
19. R. M. Stöckle, Y. D. Suh, V. Deckert, and R. Zenobi, "Nanoscale chemical analysis by tip-enhanced Raman spectroscopy," Chem. Phys. Lett. **318,** 131–136 (2000).
20. N. Hayazawa, Y. Inouye, Z. Sekkat, and S. Kawata, "Metallized tip amplification of near-field Raman scattering," Opt. Commun. **183,** 333–336 (2000).
21. N. Hayazawa, Y. Inouye, Z. Sekkat, and S. Kawata, "Near-field Raman scattering enhanced by a metallized tip," Chem. Phys. Lett. **335,** 369–374 (2001).
22. M. Futamata and A. Bruckbauer, "ATR-SNOM-Raman spectroscopy," Chem. Phys. Lett. **341,** 425–430 (2001).
23. P. G. Gucciardi, M. Labardi, S. Gennai, F. Lazzeri, and M. Allegrini, "A versatile scanning near-field optical microscope for material science applications," Rev. Sci. Instrum. **68,** 3088–3092 (1997).
24. P. G. Gucciardi, S. Trusso, C. Vasi, S. Patanè, and M. Allegrini, "Nano-Raman imaging of CuTCNQ clusters in TCNQ thin films by scanning near-field optical microscopy," Phys. Chem. **4,** 2747–2753 (2002).
25. E. Betzig, P. L. Finn, and J. S. Weiner, "Combined shear force and near-field scanning optical microscopy," Appl. Phys. Lett. **60,** 2484–2486 (1992).
26. R. Toledo-Crow, P. C. Yang, Y. Chen, and M. Vaez-Iravani, "Near-field differential scanning optical microscope with atomic force regulation," Appl. Phys. Lett. **60,** 2957–2959 (1992).
27. K. Karrai and R. D. Grober, "Piezoelectric tip-sample distance control for near-field optical microscopes," Appl. Phys. Lett. **66,** 1842–1844 (1995).
28. J. Blochwitz, M. Pfeiffer, T. Fritz, and K. Leo, "Low voltage organic light emitting diodes featuring doped phtalocyanine as hole transport material," Appl. Phys. Lett. **73,** 729–731 (1998).
29. W. Gao and A. Kahn, "Controlled *p*-doping of zinc phtalocyanine by coevaporation with tetrafluorotetracyanoquinodimethane: a direct and inverse photoemission study," Appl. Phys. Lett. **79,** 4040–4042 (2001).
30. S. Liu, Y. Liu, P. Wu, D. Zhu, H. Tian, and K. Chen, "Characterization and electrical property of molten-grown CuTCNQ film material," Thin Solid Films **289,** 300–305 (1996).
31. B. Hecht, H. Bielefeldt, Y. Inouye, D. W. Pohl, and L. Novotny, "Facts and artifacts in near-field optical microscopy," J. Appl. Phys. **81,** 2492–2498 (1997).
32. P. G. Gucciardi and M. Colocci, "Different contrast mechanisms induced by topography artifacts in near-field optical microscopy," Appl. Phys. Lett. **79,** 1543–1545 (2001).
33. K. D. Weston, J. A. DeAro, and S. K. Buratto, "Near-field scanning optical microscopy in reflection: a study of far-field collection geometry effects," Rev. Sci. Instrum. **67,** 2924–2929 (1996).